Indian Journal of Engineering & Materials Sciences
Vol. 1, June 1994, pp. 135-148

# Three-dimensional modelling of fluid flow in a four-stroke compression ignition engine

D Mohan Krishna, K Rajagopal, P Srinivasa Rao & V Ganesan
Department of Mechanical Engineering, Indian Institute of Technology, Madras 600 036, India

Received 5 June 1993; accepted 4 January 1994

This paper presents the analysis of three-dimensional calculations of flow field development in a four-stroke compression ignition (CI) engine during the compression process. The calculations are performed with a modified multidimensional arbitrary mesh using finite difference hydrodynamic model. A post processor has been developed to generate in-cylinder flow characteristics. Computations are carried out with a computing mesh of 4152 cells for a crank angle duration of 90° requiring 17000 s of CPU time on a SIEMENS 32 bit mainframe computer. Results reveal an increase in swirl velocities and decrease in axial velocity of the fluid. Formation of squish induced vortices are observed near TDC. A comparison of average cylinder pressure obtained through three-dimensional computations and experimental values from a motored engine showed good agreement validating the prediction.

In a four-stroke CI engine the combustion process directly influences not only the performance and emissions of the engine but also many other thermal and mechanical details of engine characteristics. There is a continuous interest in the studies of combustion phenomena so that delicate balance between fuel economy, emissions and performance could be achieved.

The process of combustion is always controlled by the fuel-air mixing and the flow field development established during compression near TDC. The compression process, combined with the configuration of the combustion chamber helps in developing a turbulent flow field and to enhance the fluid motion at a point in the engine cycle where it is mostly needed, the point of ignition. This turbulent flow field enables proper mixing of the fuel with air and prepares a mixture environment that will be conducive for ignition. The flow patterns and the temperature distribution within the cylinder also affect heat transfer to cylinder walls and piston crown. Hence a good understanding of the fluid dynamics within the cylinder during the compression process is essential in designing the engines with most attractive performance and emission characteristics.

The research in understanding engine flows comes from both experimental measurements and numerical computations. Experimental techniques include applications of hot-wire anemometry[1-4] and laser Doppler anemometry[5-7] for flow analysis at specific locations in engine cylinder. To obtain knowledge from these traditional as well as advanced experimental techniques is time-consuming. Expensive experiments and specific engine designs do not lead to similarity laws for predicting the characteristics of a different design. Therefore, with the advent of computational tools, the field of computer simulation of engine flow processes is now developing rapidly. The present work deals with the three-dimensional simulation of in-cylinder flows during the compression process in a four-stroke CI engine.

## Numerical Model

The air flow within the cylinder is extremely complex and three-dimensional. They are unsteady and turbulent in nature as a result of reciprocating piston movement. In addition, when the liquid fuel is injected into the cylinder phase change is also involved. The flow becomes reactive when combustion takes place. Simulation of the above flows through solving concerned partial differential equations demands excessive amounts of computing resources. In addition to these limitations, problems do exist in terms of numerical accuracy and ability to represent the mechanisms for turbulence, fuel droplet evaporation and chemical kinetics during combustion.

In the present work, KIVA, a time-marching three-dimensional, finite difference program developed by Amsden and others[8,9] is modified and used to study the flow field during the compression process. This program solves the three-di-

mensional, unsteady equations of motion of a chemically reactive mixture of ideal gases. It can also solve for the dynamics of liquid fuel spray and the coupling between the spray and the gas. This program is specifically written for super computers and makes extensive use of vector processor. The following sections present the basic governing equations and a scheme of solution.

**Governing equations**

The governing equations are written in vector notation. The unit vectors in the x-, y- and z-directions are denoted by **i**, **j**, and **k** respectively. The position vector **x** is defined by

$$\mathbf{x} = x\mathbf{i} + y\mathbf{j} + z\mathbf{k} \qquad \ldots (1)$$

The vector operator $\nabla$ is given by

$$\nabla = \mathbf{i}\frac{\partial}{\partial x} + \mathbf{j}\frac{\partial}{\partial y} + \mathbf{k}\frac{\partial}{\partial z} \qquad \ldots (2)$$

and the fluid velocity vector **u** is given by

$$\mathbf{u} = u(x, y, z, t)\mathbf{i} + v(x, y, z, t)\mathbf{j} + w(x, y, z, t)\mathbf{k} \quad \ldots (3)$$

where $t$ is the time. It is to be noted that $x \neq |\mathbf{x}|$ and $u \neq |\mathbf{u}|$.

Since the program solves the equations of motion for fluid along with those for spray droplets and chemical kinetics, equations of motion for gas phase alone are presented here. However, the details of the spray dynamics and chemical reactions are as given by Amsden and others[8,9].

*Equations of motion for the fluid phase*—The total mass density $\rho$ of the fluid (excluding the mass of the spray droplets) is given by

$$\rho = \sum_m \rho_m \qquad \ldots (4)$$

where $\rho_m$ is the partial mass density of the species $m$.

The continuity equation for species $m$ is

$$\frac{\partial \rho_m}{\partial t} + \nabla \cdot (\rho_m \mathbf{u}) = \nabla \cdot [\rho D \nabla(\rho_m/\rho)] + \dot{\rho}_m^C + \dot{\rho}_s \delta_{ml} \qquad \ldots (5)$$

where $D$ is the species diffusivity (assumed to be same for all species), $\dot{\rho}_m^C$ is the rate of change of $\rho_m$ due to chemical reactions (not considered in the present work), $\dot{\rho}_s$ is the rate of change of $\rho_l$ due to spray evaporation or condensation (not considered), $\delta_{ij}$ is the Kronecker delta, and $l$ is the species of which the spray droplets are composed.

The total fluid density $\rho$ satisfies the equation

$$\frac{\partial \rho}{\partial t} + \nabla \cdot (\rho \mathbf{u}) = \dot{\rho}_s \qquad \ldots (6)$$

The momentum equation for the fluid mixture is

$$\frac{\partial}{\partial t}(\rho \mathbf{u}) + \nabla \cdot (\rho \mathbf{u}\mathbf{u}) = -\nabla_p + \nabla \cdot \boldsymbol{\sigma} + \mathbf{F}_s \qquad \ldots (7)$$

where $p$ is the fluid pressure, $\boldsymbol{\sigma}$ is the viscous stress tensor and $\mathbf{F}_s$ is the momentum per unit volume per unit time transferred from the spray droplets to the fluid (not considered in the present work).

The stress tensor is given by

$$\boldsymbol{\sigma} = \mu[(\nabla \mathbf{u}) + (\nabla \mathbf{u})^T] + \lambda(\nabla \cdot \mathbf{u})\boldsymbol{I} \qquad \ldots (8)$$

where $\mu$ and $\lambda$ are the first and second viscosity coefficients, $\boldsymbol{I}$ is the unit dyadic and superscript $T$ denotes the transpose.

The internal energy equation is

$$\frac{\partial}{\partial t}(\rho I) + \nabla \cdot (\rho I \mathbf{u}) = -p\nabla \cdot \mathbf{u} + \boldsymbol{\sigma} : \nabla \mathbf{u} - \nabla \cdot \mathbf{J} + \dot{Q}_C + \dot{Q}_s + \dot{Q}_T \qquad \ldots (9)$$

where $I$ is the specific internal energy of the fluid (exclusive of the chemical energy), **J** is the heat flux vector, $\dot{Q}_C$ and $\dot{Q}_s$ are the source terms associated with the chemical reactions and spray droplets (not considered), and $\dot{Q}_T$ is a source term associated with the turbulence model (specified in turbulence model).

The heat flux is given by

$$\mathbf{J} = -k\nabla T - \rho D \sum_m h_m \nabla (\rho_m/\rho) \qquad \ldots (10)$$

where $k$ is the thermal conductivity, $T$ is the absolute temperature, and $h_m$ is the partial specific enthalpy of species $m$.

The state relations in the model are assumed to be those of an ideal gas mixture. Hence

$$p = R_g T \sum_m (\rho_m/\hat{W}_m) \qquad \ldots (11)$$

$$I(T) = \sum_m (\rho_m/\rho) I_m(T) \qquad \ldots (12)$$

$$c_v(T) = \sum_m (\rho_m/\rho) c_{vm}(T) \qquad \ldots (13)$$

$$h_m(T) = I_m(T) + R_g T/\hat{W}_m \qquad \ldots (14)$$

where $I_m(T)$ is the partial specific internal energy for species $m$, $c_{vm}(T)$ is the specific heat at constant volume for species $m$, $c_v$ is the mixture

specific heat at constant volume, $R_g$ is the universal gas constant, and $\hat{W}_m$ is the molecular weight of species $m$.

*Turbulence model*—The effects of turbulence are represented by a subgrid scale turbulence model which is a generalisation of the original algebraic subgrid scale model. This model uses the same above given laminar equations with suitable averaging. In the process of averaging, flow variables are separated into mean and fluctuating components. The averaged equations are considerably simpler if the mean values are mass weighed. The fluctuation terms are generally modelled by the gradient-flux approximation.

In this approximation the averaged turbulent equations become identical in form to be laminar ones; the transport coefficients (i.e. viscosity, thermal conductivity and species diffusivity) are simply replaced by the appropriate turbulent values. Hence the above equations are used when the flow is turbulent but with turbulent contributions added to the laminar values of the transport coefficients. The transport coefficients in the model are as follows:

$$\mu = \rho\nu_0 + \mu_{air} + \mu_t$$
$$K = \mu C_p / Pr$$
$$D = \mu/(\rho Sc) \qquad \ldots (15)$$

where $\nu_0$ is called constant uniform background turbulent diffusivity, $\mu_{air} = A_1 T^{3/2}/(T + A_2)$ where $A_1$ and $A_2$ are constants, $\mu_t$ is a subgrid scale turbulent viscosity defined below, $Pr$ is the Prandtl number, and $Sc$ is the Schmidt number. Both $Pr$ and $Sc$ are taken as constants.

The subgrid scale turbulent viscosity $\mu_t$ is given by

$$\mu_t = A\rho L q^{1/2} \qquad \ldots (16)$$

where $A$ is a constant of the order of 0.05, $L$ is a characteristic length of order twice the length of a typical finite-difference cell side and $q$ is the subgrid scale turbulent kinetic energy. The latter satisfies the transport equation given below:

$$\frac{\partial}{\partial t}(\rho q) + \nabla \cdot (\rho q \mathbf{u}) = -(2/3)\rho q \nabla \cdot \mathbf{u} + \sigma : \nabla \cdot \mathbf{u}$$
$$+ \nabla \cdot (\mu \nabla q) - \hat{D}\rho L^{-1} q^{3/2} + \dot{W}_s \qquad \ldots (17)$$

where $\hat{D}$ is a constant of order unity. $W_s$ is the source term (not considered in the present work) due to the interaction between spray droplets and gas.

The turbulence source term $\dot{Q}_T$ in the internal energy equations is given by the following equation:

$$\dot{Q}_T = A_0(\hat{D}\rho L^{-1} q^{3/2} - \sigma : \nabla \mathbf{u}) \qquad \ldots (18)$$

where $A_0 = 1$ when the turbulence model is in use and $A_0 = 0$ otherwise.

The dynamics of atomized fuel sprays are represented by a Monte Carlo based discrete particle technique, by Ducowicz[10]. The spray is considered to be composed of discrete computational particles each of which represents a group of droplets of similar physical properties. The distribution function in droplet size, velocity, spray pattern and temperature by the fuel injector is statistically sampled and the resulting particles are followed as they locally interact and exchange mass, momentum and energy with the gas. The model accounts for turbulence effects and interactions between droplets but other thick spray effects are neglected.

Chemical reactions that can be considered through the KIVA are arbitrary in number and are limited only by computer memory and time. Chemical reactions are treated by a procedure that identifies between slow reactions which proceed kinetically and fast reactions which are assumed to be in equilibrium.

However, in the present analysis only flow modelling during compression process is considered. Hence equations regarding spray dynamics and chemical reactions are not presented in this paper.

#### Numerical scheme

The model solves the finite difference approximations to the governing equations mentioned in the earlier sections. In this part of the paper some general features of the numerical scheme are explained briefly. The complete information of the governing equations, their difference equations and their solutions are available in KIVA Report by Amsden and others[8,9].

*Temporal differencing*—The temporal differencing is performed with respect to a sequence of discrete times, (cycles), $t^n$ ($n = 0, 1, 2 \ldots$). The time interval $\Delta t_n = t^{n+1} - t^n$ is the time step and the integer $n$ is the cycle number. The value of each dependent variable of each cycle is calculated from that of the previous cycle. The temporal differencing scheme is explicit, which uses an acoustic subcycling method[11] for calculating flows efficiently at low Mach numbers. The cycle number is displayed as a superscript so that $Q^n$ denotes the difference approximation to the quantity $Q$ at

time $t^n$. The difference approximation to the derivative

$\frac{\partial Q}{\partial t}$ is

$(Q^{n+1} - Q^n)/\Delta t$

A cycle that is the advancement of variable from time $t^n$ to time $t^{n+1}$, is performed in three stages. Phase A is the calculation of the effects of most terms in the governing equations other than pressure and convection terms. Phase B is a Lagrangian subcycling calculation in which the vortices are temporarily assumed to move with the local fluid velocity. This phase is also concerned with the calculation of the terms related to acoustic waves (pressure forces and $pdV$ work terms) and the drag forces between spray particles and fluid. Phase C is the rezone phase. In this phase the convective transport associated with moving the vertices from their phase B locations to their final locations is calculated. This transport arises because of the motion of the fluid relative to mesh.

*Spatial differencing*—Spatial differencing is formed with respect to a generalized three-dimensional finite difference mesh that subdivides the region of interest into a number of small cells. The corners of the cells (vertices) may be arbitrarily specified as functions of time, thereby allowing a Lagrangian, Eulerian or a mixed description[12,13]. This feature is particularly useful for representing curve/moving boundaries. Spatial difference approximations are constructed by the control-volume or integral balance approach[12-14] which largely preserves the local conservation properties of the differential equations. The procedure that is used for spatial differencing is to difference the basic equations in integral form, with the volume of a typical cell used as control volume and the divergence terms transformed into surface integral using divergence theorem[14].

*State relations*—The internal energy of species is obtained from the JANAF tables[15] are stored in tabular form at intervals of 100 K. A simple linear interpolation is used to determine the species internal energy at temperatures within the range of the tables. Specific heats at constant volume for species are approximated by the differences between adjacent tabular values of species internal energy at corresponding temperatures divided by 100 K.

For one of the species, liquid octane fuel, data like latent heat of fuel, internal energy and equilibrium vapour pressure are stored in the tabular form.

**Boundary conditions**

Two types of boundary conditions are required to be provided to calculate the flow field computational domain. They are temperature and velocity boundary conditions. In the present work the law of the wall boundary conditions[8] is considered to resolve boundary layers near the solid walls while calculating the velocities as shown below:

(i) when the wall is flat (as in the case of flat portion of a piston, or the surface of the cylinder head), the components of tangential velocity are calculated.

(ii) when the wall is having curvature in one direction (as in the case of the cylinder liner), the component of tangential velocity in the direction of no curvature, is set equal to the same component at the next closest cell corner (but not on the wall). The other component of the tangential velocity, i.e., in the direction of curvature is set to zero.

(iii) when the wall is curved in both principal directions (like in the case of hemispherical bowl) both components of tangential velocity are set to zero.

The normal velocity is always set equal to the velocity of the corresponding wall.

From this velocity boundary condition wall shear stress is deduced at the grid points closest to the wall. Then wall heat loss is obtained using Reynolds analogy formula. With fixed wall temperature boundary condition heat flux is calculated and coupled to energy equation.

## Computer Program

The computer program consists of a set of primary and secondary subroutines controlled by a short main program. This program is written for use in CRAY-1 64 bit super computer using the CRAY Fortran Compiler (CFT). The Fortran code contains statements peculiar to CFT that permits vectorization of the code to run very fast. The code also requires many system subroutines during execution. For post processing the local field variables the system uses a Graphic Software that it integrated with Fortran code.

*Modifications of the code*—The code, that is specifically developed for the above super computer is fully implemented in the SIEMENS-32 Bit Computer. This system, operating under time sharing environment provides a FORTRAN com-

piler. However, the BS 2000 operating system of SIEMENS does not offer any postprocessing utilities.

The code was fully modified so that it will be suitable to the SIEMENS environment. The modifications include a complete change in the structure of the common blocks, provision of system subroutines, logical routines that are available on CRAY.

In addition to this, provision is made to run the program in segments. Since the program is used to solve time-marching three-dimensional flow problems and the system is non-CRAY one, the run cannot be completed in a single day. Hence modules are developed to dump the common block and equivalence variables at a required time (or crank angle position). For subsequent calculations the run can be restarted from the previous crank angle position.

*Development of post-processor*—The prediction procedure generates a huge amount of data at any position of the piston. The global parameters like average cylinder pressure, total angular momentum, etc., can be analysed for through ordinary x-y plots. However, the analysis of local field variables (like velocities in x-, y- and z-directions, temperatures, TKE) at each position of the piston can be carried out only through a specifically developed post-processor.

The post processing software (PPS) is developed on a 16 bit graphic work station which operates under UNIX 2 operating environment. The post processor developed in this work using the above utilities allows viewing and plotting the following jobs both in horizontal and axial planes of the engine cylinder. (i) Computing mesh representation in two-dimensional and three-dimensional views, (ii) Velocity vector field representation, (iii) Contour mapping of scalar variables like temperature, TKE, etc. and (iv) Spray particle distribution projection.

## Selection of Computational Grid

In fluid flow computations, the grid size will be employed to approximate spatial variations in computational domain will play an important role in arriving at plausible results. By using high density grids numerical truncation errors can be reduced to acceptable levels. But increasing the grid density increases computational time and space considerably. So a certain compromisation is required between the computing resources and the selection of best possible grid size is three-dimensions.

In arriving at the best possible grid size, the grid size is varied in two directions, namely axial and tangential direction of the computing mesh. In the first case where the grid size is varied only in axial direction by varying the number of cells, NZ, as 10, 13 and 16. The number of cells in radial direction, NX, and tangential direction, NY, are kept constant at 13 and 16, respectively. In the second case, the number of cells in tangential direction (NY) is changed from 12 to 16. NX and NZ are kept constant at 13 and 19, respectively.

It may be noted that the number of cells is varied in the NZ direction in which the piston movement takes place. Variation of cells in tangential direction, NY, is to account for three-dimensional effect. In the radial direction the number of cells, NX, is chosen to keep the truncation errors to the minimum.

For the grid independence test the computations are commenced at 90° bTDC and are continued for a crank angle duration of 10°, i.e., upto 80° bTDC during the compression process with bowl in piston configuration.

An examination of the local field variations indicated that there is no variation in the velocity field[16]. The differences in maximum velocity components are of higher magnitude when grid size is varied in axial direction. Increasing the grid size also reduced the peak values of velocity components.

Table 1 shows the computational time that was consumed for each test case. It can be observed that the grid refinement demands excessive amount of CPU time. With these points in mind, from all sizes of grids considered in both cases, i.e. $13 \times 16 \times 10$; $13 \times 16 \times 13$; $13 \times 16 \times 16$ (case 1) and $13 \times 12 \times 19$; $13 \times 16 \times 19$ the grid chosen is $13 \times 16 \times 19$. This computations grid is employed for the 3-D computations of comparison process.

*Details of computations of compression process*—The main objective of the present work is to study the in-cylinder fluid mechanics during compression process in a CI engine. The piston is

Table 1—CPU time history for different grid sizes

| Gride size $NX \times NY \times NZ$ | Computational time s |
|---|---|
| $13 \times 16 \times 10$ | 1091.1 |
| $13 \times 16 \times 13$ | 1479.6 |
| $13 \times 16 \times 16$ | 1738.6 |
| $13 \times 12 \times 19$ | 1564.0 |
| $13 \times 16 \times 19$ | 2153.2 |

Table 2—Engine details

| Engine Configuration | | Piston Configuration | |
|---|---|---|---|
| Bore | 8.75 cm | Hemispherical Bowl-in-piston | |
| Stroke | 11.00 cm | Bowl radius | 2.53 cm |
| Squish | 1.50 cm | Operating Conditions | |
| Connecting rod length | 23.20 cm | Engine speed | 1500 rpm |
| | | Swirl | 3 (clockwise) |

provided with a fuel injection or ignition processes are considered in this work. The engine configuration, operating conditions, bowl configuration and other details considered for this study are given in Table 2.

During compression process, actual compression begins at 146° bTDC (inlet valve closure) and proceeds upto TDC. However, initial part of compression (upto 90° bTDC) produces a small change in in-cylinder as well as global properties like pressure, etc. The stage of compression from 90° bTDC to TDC is an important one where fuel injection and ignition will take place. Due to this reason the significant part of compression process, i.e., from 90° bTDC to TDC is considered for the present study.

The other important point in calculating three-dimensional flows, particularly of engine flows, is that it consumes excessive amount of computing time and memory. For the present calculations, i.e., from 90° bTDC to TDC it takes 4.716 h of CPU time. This is the other reason why the computations are carried out only for this significant stage of compression.

The calculations are performed with an initial air swirl ratio (at 90° bTDC) of 3, with a charge temperature of 400 K and wall temperature of 400 K. Fig. 1 shows the top view, elevation and pictorial view of the computational grid at this point (89.84° bTDC). The results are analyzed in terms of local field parameters (velocity vectors and contour plots for temperature and TKE both in horizontal and axial planes of the engine cylinder), which were generated through PPS. In addition to these parameters, vital global parameters like average cylinder pressure and total angular momentum are also considered for analysis.

An attempt has been made to compare the average cylinder pressure history with that of experimental one, both qualitatively and quantitatively.

## Results and Discussions

The local and global variables are stored at every 10° crank angle duration and processed for data analysis through PPS. Flow parameters are

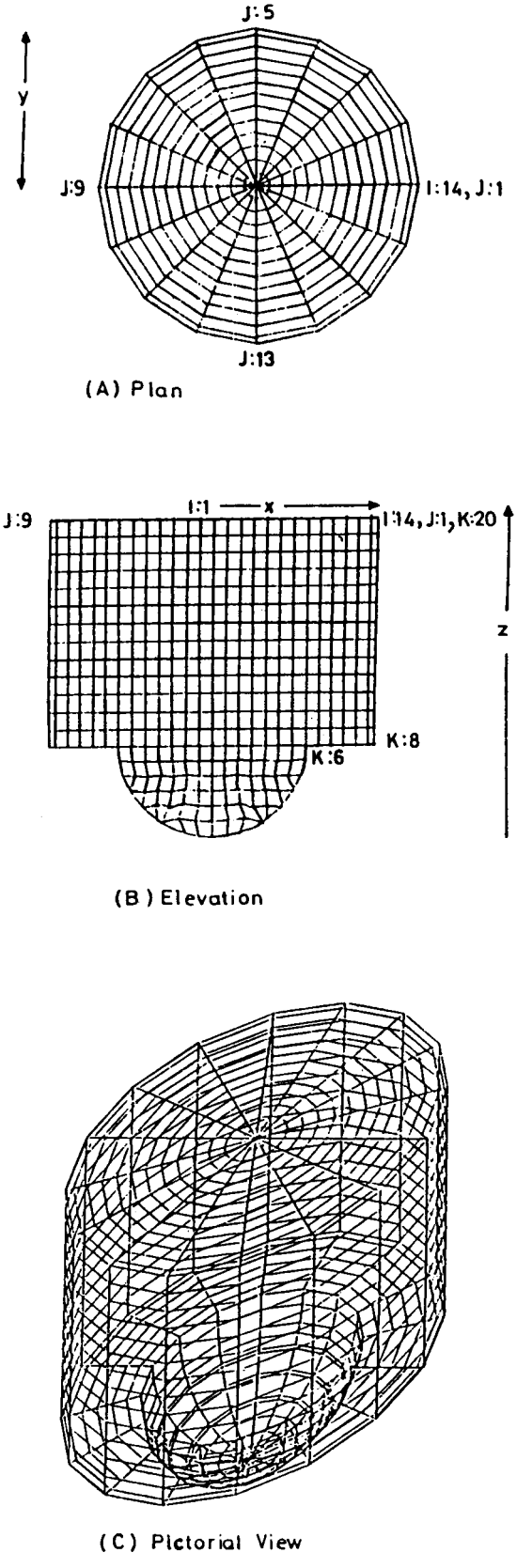


Fig. 1—Details of the computational grid

analyzed at 80°, 60°, 20° and 10° before and very close to TDC (0.02°).

In cylinder flow predictions and analysis are done at the same plane irrespective of the piston movement in order to make the comparison meaningful. Horizontal planes K6 and K8 and vertical planes J1 and J9 (diametrically opposite planes in elevation) are selected for the flow analysis. Important point is that as the piston moves towards TDC the position of K8 plane (the plane that is immediately above the piston surface) also varies. But it is still close to the piston surface.

*Velocity field development during compression*—Fig. 2 show the plan view of velocity vectors in K6 plane which is within the bowl. In this plane, at 80° bTDC, the average velocity increases linearly from bowl center to bowl rim. As the piston moves towards TDC, the magnitude of $U$ (velocity component in x-direction) and $V$ (velocity in y-direction) increase rapidly due to decrease in the combustion chamber volume. As expected the $U_{max}$ and $V_{max}$ start increasing as the piston moves towards TDC, showing an increase in swirl (an organised rotation).

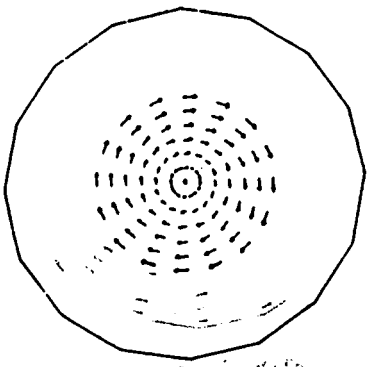

(a) Crank angle 80°C bTDC ($U_{max}$ = 10.144 m/s, $V_{max}$ = 10.144 m/s)

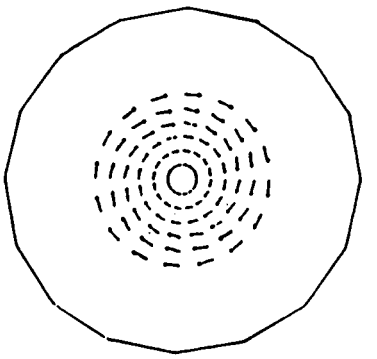

(b) Crank angle 60° bTDC ($U_{max}$ = 11.845 m/s, $V_{max}$ = 11.845 m/s)

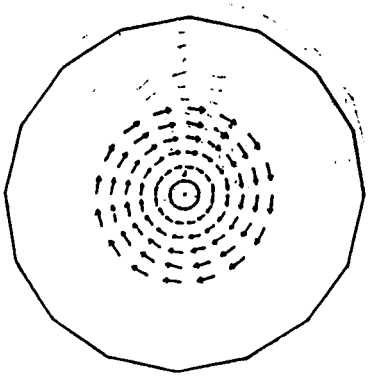

(c) Crank angle 20° bTDC ($U_{max}$ = 17.571 m/s, $V_{max}$ = 17.708 m/s)

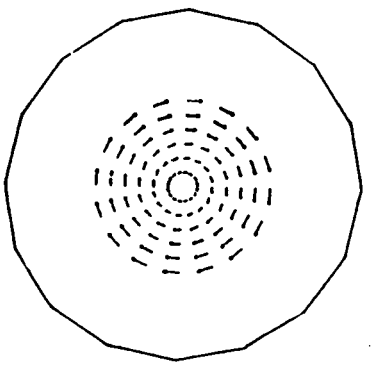

(d) Crank angle 10° bTDC ($U_{max}$ = 25.13 m/s, $V_{max}$ = 25.349 m/s)

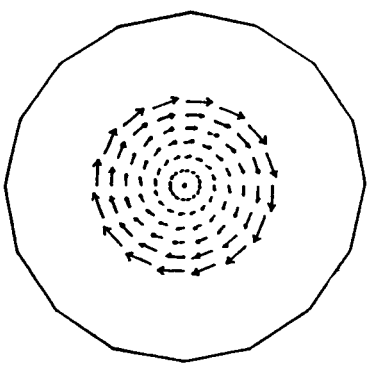

(e) Crank angle 0.02° aTDC ($U_{max}$ = 33.719 m/s , $V_{max}$ = 33.835 m/s)

Fig. 2—Velocity vectors in K6 horizontal plane

Fig. 3 gives the details of the velocity field at K8 plane. This plane is just above the piston surface. From this figure, the flow field within the piston bowl can also be observed. At 80° (Fig. 3a) there seems to be a uniform rotation of the flow field. Here, the velocity profile increases gradually from center to the cylinder wall. As the piston moves towards TDC it is clearly seen that swirl velocity within the bowl increases towards the wall and outside the bowl the velocity decreases and the air is squeezed into the bowl.

Fig. 4 shows the variation of total angular momentum with respect to crank angle during the compression process. It clearly shows the angular momentum decays continuously as the compression progresses. This is due to the friction at walls and turbulence decay within the fluid[17]. To conserve angular momentum, the swirl velocities increase. In bowl-in-pistons the increase in swirl velocities is greater compared to flat pistons. The decay in total angular momentum is more from 40° bTDC onwards showing rapid increase in

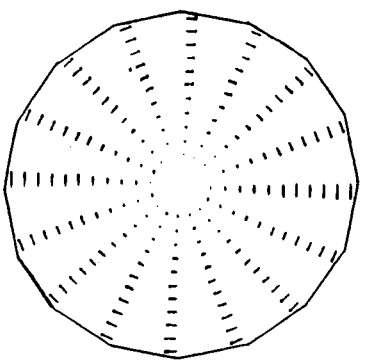

(a) Crank angle 80° bTDC ($U_{max}$ = 19.54 M0s, $V_{max}$ = 19.552 m/s)

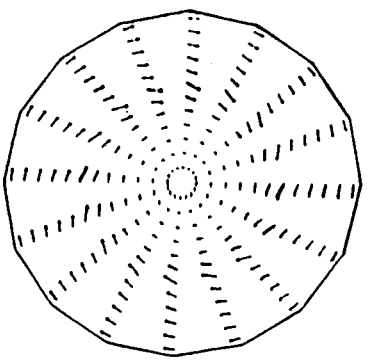

(b) Crank angle 60° bTDC ($U_{max}$ = 27.742 m/s, $V_{max}$ = 8.02 m/s)

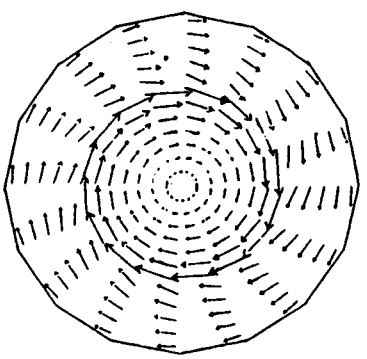

(c) Crank angle 20° bTDC ($U_{max}$ = 47.086 m/s, $V_{max}$ = 48.027 m/s)

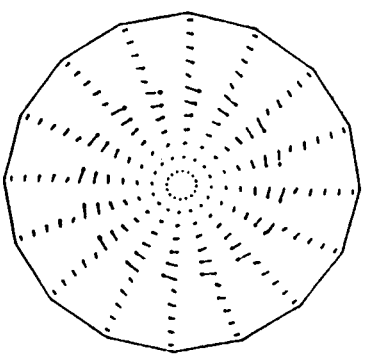

(d) Crank angle 10° bTDC ($U_{max}$ = 57.980 m/s, $V_{max}$ = 58.661 m/s)

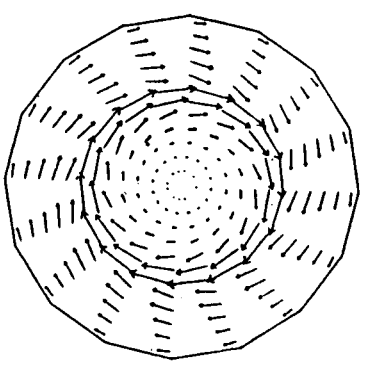

(e) Crank angle 0.02° aTDC ($U_{max}$ = 49.381 m/s, $V_{max}$ = 49.502 m/s)

Fig. 3—Velocity vectors in K8 horizontal plane

swirl velocities from 20° bTDC onwards.

Fig. 5 shows the variation of velocity vectors in J1 and J9 axial planes. Squish flow, an important feature of the flow during compression, can be observed from these figures. Squish flow is defined as the radially inward or transverse gas motion that occurs during the compression stroke. At 80° bTDC (Fig. 5a) it is observed that the velocity vectors move along with piston. At 60° bTDC it can be seen that the flow is tending to enter the bowl. At 20° bTDC (Fig. 5c), due to the piston movement towards the cylinder head, less space is available and the fluid is pushed into the bowl. At 10° bTDC formation of vortices in the bowl is clearly observed. These vortices are same in size, symmetric about the cylinder axis and are opposite in direction. Increased velocities near the bowl rim are also observed. Thus the formation of vortices as a result of swirl-squish interaction are clearly observed. The vortex size is observed to be larger by about 20. The axial component of velocity, $W_{max}$, decreases following the piston motion towards TDC during compression.

*Temperature field development*—Temperature contours plots are drawn at the same crank angle positions where velocity are presented. Fig. 6 show the temperature contours in K8 horizontal plane of the engine cylinder during compression. At 80° bTDC (Fig. 6a) the highest and lowest temperatures shown are 427 and 425K with a difference of 2K. This temperature difference increases as the piston moves towards TDC. This increase is moderate at 60° bTDC (8K). From 20° bTDC to 0.02° aTDC (Fig. 6e) this difference increases from 15 to 66K. At any position of the

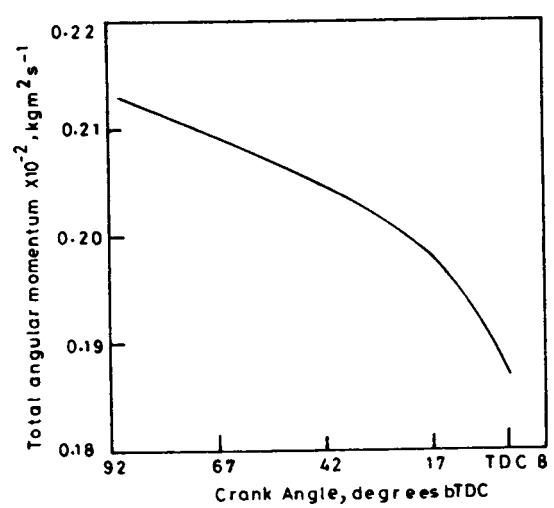


Fig. 4—Variation of angular momentum

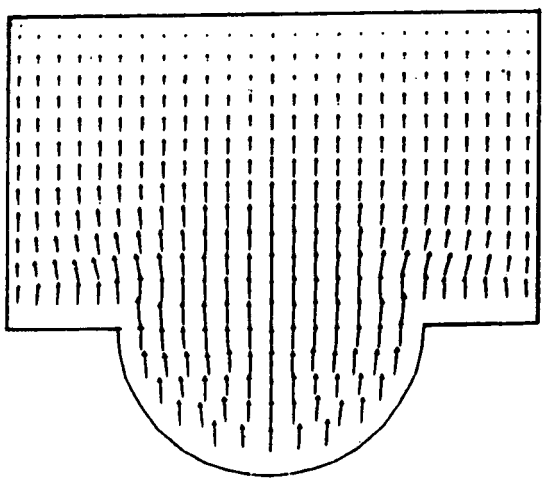

(a) Crank angle 80° bTDC ($U_{max}$ = 2.304 m/s, $W_{max}$ = 11.501 m/s)

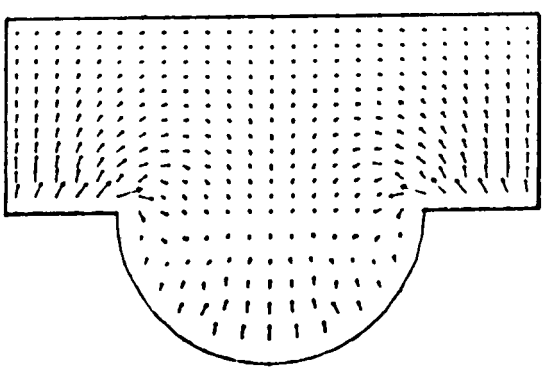

(b) Crank angle 60° bTDC ($U_{max}$ = 13.166 m/s, $W_{max}$ = 8.361 m/s)

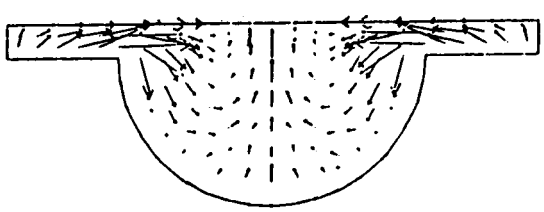

(c) Crank angle 20° bTDC ($U_{max}$ = 15.320 m/s, $W_{max}$ = 8.340 m/s)

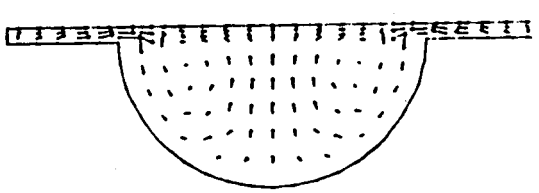

(d) Crank angle 10° bTDC ($U_{max}$ = 16.034 m/s, $W_{max}$ = 7.223 m/s)

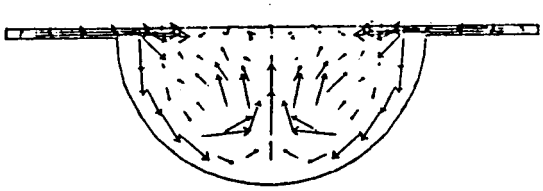

(e) Crank angle 0.02° aTDC ($U_{max}$ = 11.486 m/s, $W_{max}$ = 7.647 m/s)

Fig. 5—Velocity vectors in J1-J9 axial planes

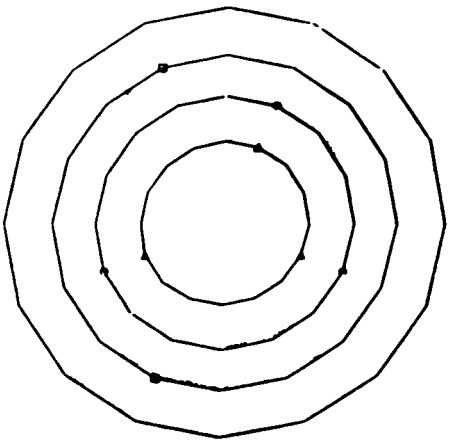

(a) Crank angle 80° bTDC (□-425, ○-426, Δ-427)

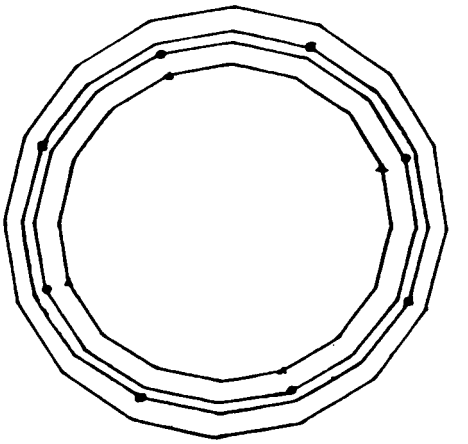

(b) Crank angle 60° bTDC (□-494, ○-495, Δ-496)

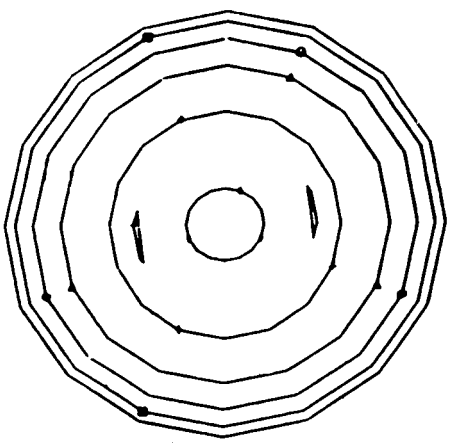

(c) Crank angle 20° bTDC (□-760, ○-765, Δ-770, +-772, ◇-775)

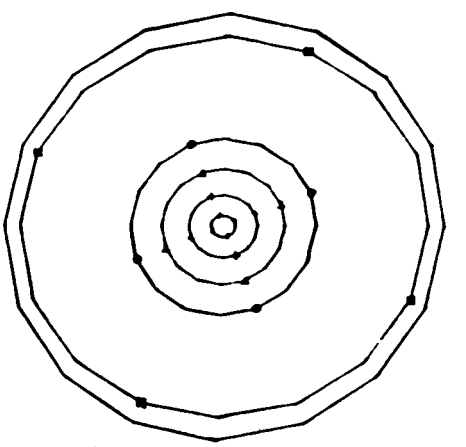

(d) Crank angle 10° bTDC (□-826, ○-840, Δ-850, +-860, ◇-865)

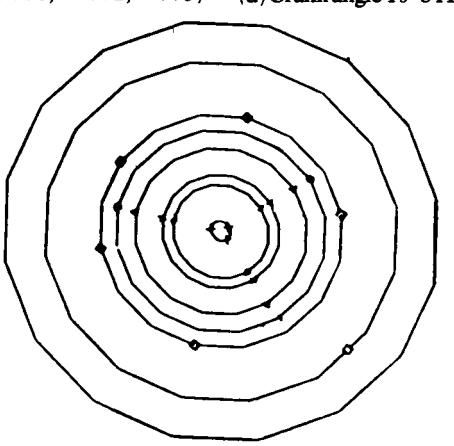

(e) Crank angle 0.02° aTDC (□-835, ○-850, Δ-865, +-885, ◇- 890, ×-899)

Fig. 6—Temperature contours in K8 horizontal plane

piston the temperature contours are symmetric about the cylinder axis. Maximum temperature is located at the center of the bowl and reduces gradually towards cylinder wall. The observations for K6 and K7 planes also indicate a very similar trend in temperature contours[16].

In axial planes, Fig. 7, the temperature contours exhibit the same behaviour as seen in respect of horizontal planes. It is very clearly seen that the peak temperatures always occur within the bowl. At TDC a peak temperature of 902 K is observed. It is also observed that the temperature contours obtained for J5 and J13 (diametrically opposite) axial planes indicate the same trend in their variation as to that of J1 and J9 axial planes.

The nature of temperature profiles in axial planes and their trend support the fact that compression results in higher temperatures and pro-

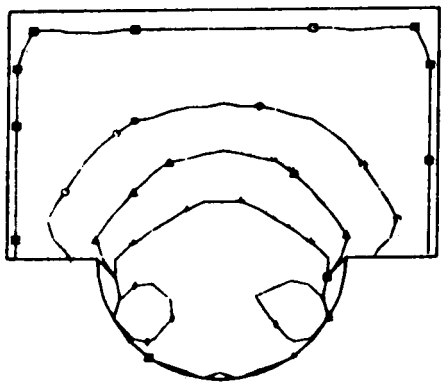

(a) Crank angle 80° bTDC (□-424, ○-425, Δ-426, +-427, ◇-428)

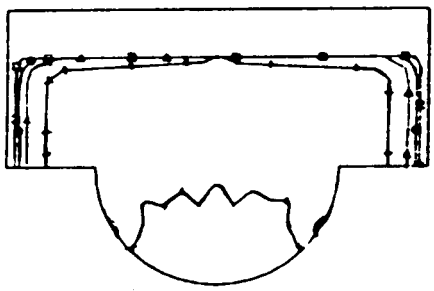

(b) Crank angle 60° bTDC (□-493, ○-494, Δ-495, +-496, ◇-497)

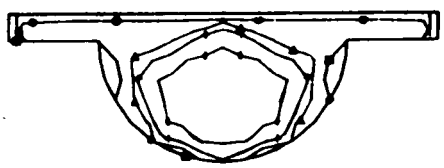

(c) Crank angle 20° bTDC (□-715, ○-760, Δ-776, +-778, ◇-780)

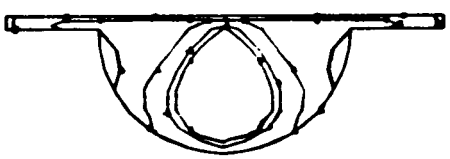

(d) Crank angle 10° bTDC (□-725, ○-830, Δ-862, +-867, ◇-868)

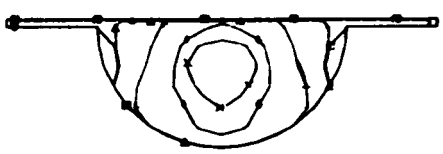

(e) Crank angle 0.02° aTDC (□-725, ○-800, Δ-850, +-885, ◇-900, ×-903)

Fig. 7—Temperature contours in J1-J9 axial planes

vide a good environment for proper evaporation of the injected fuel.

*Turbulence characteristics*—The turbulent characteristics of flow field are evaluated through solving transportation equation for turbulent kinetic energy (TKE). Contours of turbulent kinetic energy are plotted both in horizontal and axial planes of the engines during compression process.

Fig. 8 shows the turbulent kinetic energy contours during the compression process in K8 plane. At 80° bTDC the center of the cylinder has the lowest TKE level. As the radius increases TKE also increases and reaches a maximum near the cylinder wall. The same trend can be observed even at 60° bTDC (Fig. 8b).

From 20° bTDC onwards the peak values of TKE can be found near the bowl rim region. Here, compared to swirl the squish plays a more dominant role which is evident from the corresponding velocity vector plots. Due to squish, the flow enters the bowl resulting in TKE reaching a maximum value due to high shear action. The same trend is observed at 10° bTDC and at 0.02° bTDC. This is due to flow field affect near TDC.

TKE contours in J1 and J9 axial planes (Fig. 9) at 80° bTDC show tongue formation near the cylinder head. At the bowl-rim, the TKE contours follow the shape of the piston surface. Near the cylinder head there will be a drop in velocities due to the friction resulting in tongue formation with lower TKE levels. Due to the effect of swirling flow, peak TKEs are observed near the cylinder walls at 80° bTDC and 60° bTDC (Fig. 9b).

From 20° bTDC to TDC the squish flow seems to be predominant. It is observed that peak TKE always located at the bowl rim. This is due to the increased velocities of squish as a result of shear near the bowl rim. As the compression progresses lowest TKE contours move towards the axis of the cylinder. From 20° bTDC onwards the increase in TKE is very high. This shows that the flow field variation near TDC is of utmost importance. The TKE plots obtained for J5 and J13 axial planes are found to be symmetric and identical as those obtained for J1 and J9 planes.

*Comparison with experimental data*—The program is capable of predicting the pressure field also. From the pressure field it is possible to compute the average pressure. Since the validation of velocity field is not possible with the existing set-up the validation of the pressure history obtained from the three-dimensional computations by comparing with experimental values is carried out. The motored curve from a test engine of the same configuration as used in the computations is obtained through a signal analyser. At selected points of the motoring curve experimental data is compared with average cylinder pressure obtained by 3-D computations.

Fig. 10 shows the variation of average cylinder pressure with crank angle obtained from both experimental and computational cases during the

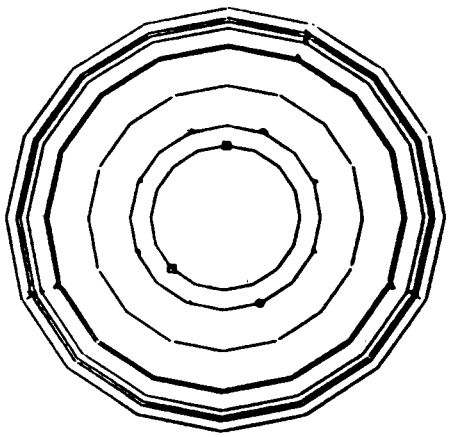

(a) Crank angle 80° bTDC (□-0.50, ○-0.75, Δ-1, +-5, ◇-10, ×-13)

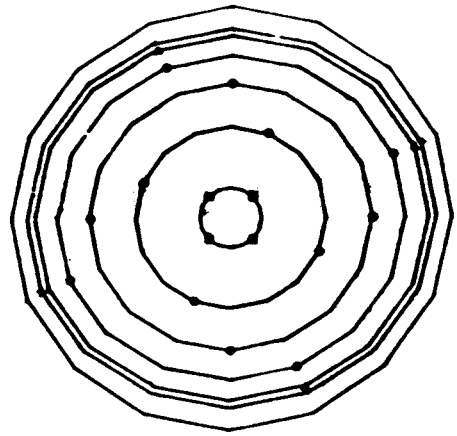

(b) Crank angle 60° bTDC (□-0.50, ○-5, Δ-10, +-15)

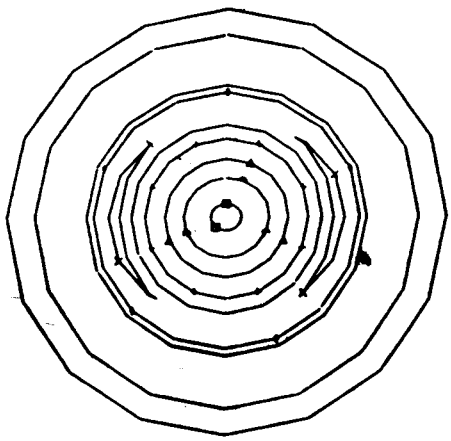

(c) Crank angle 20° bTDC (□-2, ○-5, Δ-10, +-20, ◇-30, ×-40)

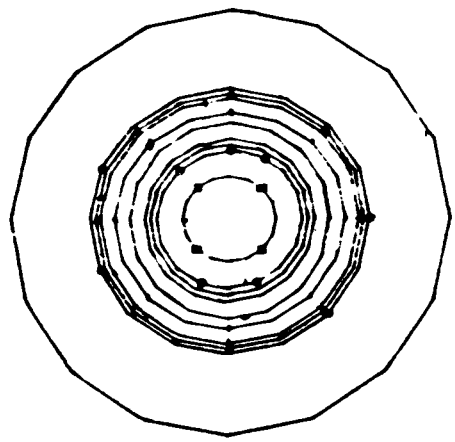

(d) Crank angle 10° bTDC (□-10, ○-50, Δ-70, +-90, ◇-120)

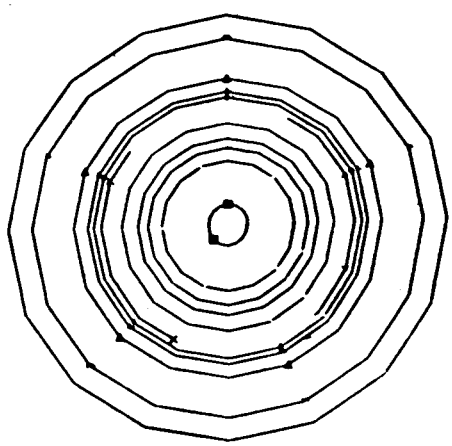

(e) Crank angle 0.02° aTDC (□-5, ○-30, Δ-60, +-90, ◇-120, ×-155)

Fig. 8—TKE contours in K8 horizontal plane

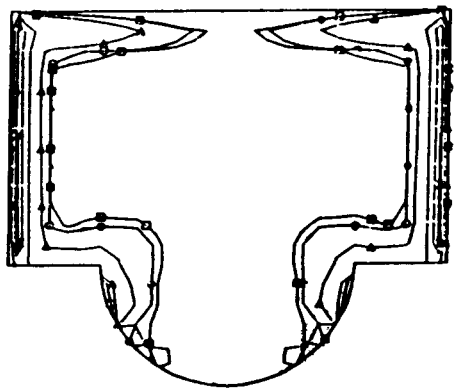

(a) Crank angle 80° bTDC (□-0.45, ○-0.50, Δ-1, +-5, ◇-10, ×-13)

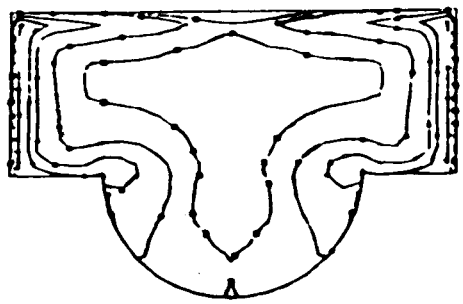

(b) Crank angle 60° bTDC (□-0.50, ○-1, Δ-1, +-10, ◇-18)

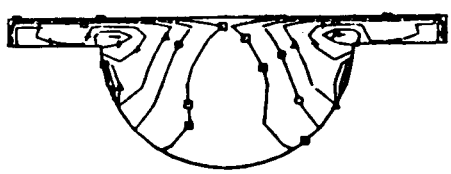

(c) Crank angle 20° bTDC (□-2, ○-5, Δ-10, +-20, ◇-30, ×-40)

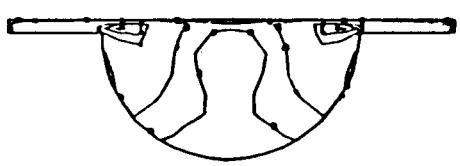

(d) Crank angle 10° bTDC (□-3, ○-10, Δ-80, +-100, ◇-120)

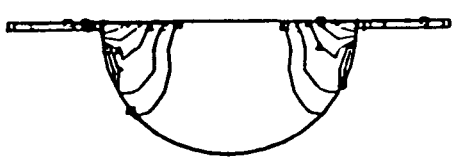

(e) Crank angle 0.02° aTDC (□-14.5, ○-30, Δ-60, +-90, ◇-120, ×-155)

Fig. 9—TKE contours in J1-J9 axial planes

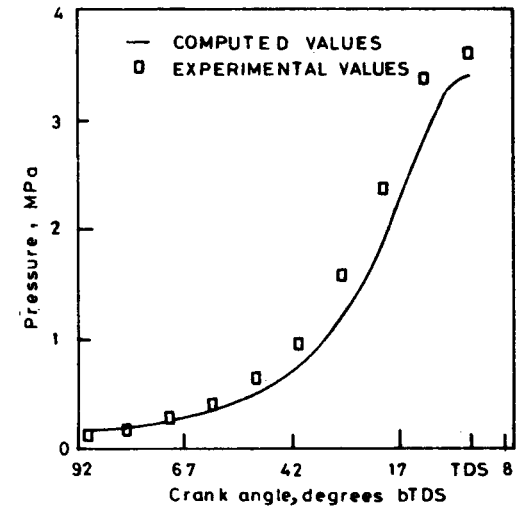


Fig. 10—Comparison of cylinder pressure from experiments and computations

compression process from 90° bTDC to TDC. The graph indicates that the predicted values of average cylinder pressure show a very good agreement with measured values. The computed pressure has slightly lower values compared to experimental values. This difference increases the compression process progresses and reaches a maximum of 3.5 per cent of experimental values. The reason for computed values being lower may be attributed to the input value of the initial charge temperature.

## Conclusions

Three-dimensional analysis of the flow field is carried out during the compression process of a four-stroke compression ignition engine. The flow field is analysed in terms of velocity vectors, temperature and turbulent kinetic energy contours. Some of the important global parameters like average cylinder pressure and total angular momentum are also considered for analysis. Computed pressure histories are compared with experimental data. From the foregoing analysis the following conclusions are drawn:

1 The flow field development from 90° bTDC to TDC during compression can be divided into two phases. The first phase can be observed from 90° bTDC to 40° bTDC. During this phase the swirl velocities increase moderately. Within the bowl, the charge in lower horizontal planes rotate with lower speed compared to the upper planes. Above the bowl, from piston surface to cylinder head swirl velocities reduce. In axial planes the effect of bowl is clearly seen. The axial velocity of the flow field reduces considerably as the piston towards the cylinder head.

2 The temperature contours show the expected trend of high temperature at the core and comparatively lower temperature near the cylinder wall. Turbulent kinetic energy contours reflect the property of swirling flows along with tongue formation near the cylinder head.

3 Total angular momentum varies approximately as the compression progresses from 90° bTDC to 40° bTDC.

4 In the second phase from 40° bTDC to TDC that can be termed as near TDC region, the local and global parameters change rapidly.

5 During this phase the swirl velocities increase drastically due to the presence of bowl in the piston. Squish flow is observed to be dominant in this phase. Swirl and squish interaction is also clearly seen.

6 The temperature of the charge increases rapidly and reaches a maximum. The variation of temperature within the bowl is less compared to that in the cylinder. Due to squish, the maximum TKE is always observed to be near the bowl rim.

7 Total angular momentum decays rapidly as the piston reaches TDC.

8 The predicted average cylinder pressure histories compare moderately well with the experimental data.

It is in the second phase during which the local and global parameters of the flow field vary steeply. This creates an environment that is more convenient for fuel-air mixing, evaporation and combustion.

## References


1 Williams T J & Tindal M J, *Gas flow studies in direct injection diesel engines with re-entrant combustion chambers*, SAE Paper No. 800027, 1980.

2 Subramaniyam S, Sampath S, Srinivasa Rao P & Ganesan V, *J Exp Methods Fluids*, 9 (1990) 167-174.

3 Subramaniyam S, Ganesan V & Srinivasa Rao P, *An experimental investigation of flow characteristics in the swirl chamber of a CI engine*, SAE Paper No. 910480, 1990.

4 El Tahry S H, Khalighi B & Kuzian Jr. W R, *Unsteady flow velocity measurements around an intake valve of a reciprocating engine*, SAE Paper No. 870593, 1987.

5 Dyer T M, *New experimental techniques for in-cylinder engine studies*, SAE Paper No. 850395, 1985.

6 Arcoumanis C, Green H G & Whitelaw J H, *The application of laser Rayleigh scattering to a reciprocating engine model*, SAE Paper No. 840376, 1984.

7 Jhonson S C, *Precombustion fuel/air distribution in a stratified charge engine using laser Raman spectroscopy*, SAE Paper No. 790433, 1979.

8 Amsden A A, Ramshaw J D, O'Rourke P J & Ducowicz J K, *KIVA: A computer program for two- and three-dimensional fluid flows with chemical reactions and fuel sprays*, Los Alamos National Laboratory Report No. LA-10245-MS, 1985.

9 Amsden A A, Ramshaw J D, Cloutman J D & O' Rourke P J, *Improvements and extensions to KIVA computer program*, Los Alamos National Laboratory Report No. LA-10534-MS, 1985.

10 Dukowicz J K, *J Comput Phys*, 35 (1980) 229.

11 Haselman L C, *TDC—A computer code for calculating chemically reacting hydrodynamic flows in two-dimensions*, Lawrence Livermore Laboratory, Report UCRL-52931, 1980.

12 Hirt C W, Amsden A A & Cook J L, *J Comput Phys*, 11 (1974) 227.

13 Pracht W E, *J Comput Phys*, 17 (1975) 132.

14 Stein L R, Gentry R A & Hirt C W, *Comput Methods Appl Mech Eng*, 11 (1977) 57.

15 Stull D R & Prophet H, *JANAF thermochemical tables*, 2nd Edition, (U S Department of Commerce/National Bureau of Standards), 1971.

16 Mohan Krishna D, *Multidimensional modelling of fluid flow in a four-stroke CI engine*, M S Thesis, IIT, Madras, 1990.

17 Heywood J B, *Internal combustion engine fundamentals* (McGraw Hill Series, New York), 1989.